

Waveform Tomography and its application to Marine Seismic Refraction Data

Sreeja Nag

The Indian Institute of Technology, Kharagpur

India- 721302

Summer Student Fellow, Woods Hole Oceanographic Institution

sreejanag@gmail.com

J. P. Canales

Woods Hole Oceanographic Institution,

Woods Hole, U.S.A. - 02543

Abstract

The active hydrothermal mound on the Trans-Atlantic Geotraverse (TAG) segment of the Mid-Atlantic Ridge at 26°N is located on the footwall of a long-lived, active, normal detachment fault as shown by geophysical studies. The hydrophone data from 5 ocean-bottom seismometers (OBS) deployed in the vicinity of the TAG mound were used to simulate a full waveform seismic tomographic inversion to image the velocity structure of the fault system which can provide information on fluid flow and alternation along the fault zone. The OBS data are large-offset, refracted, seismo-acoustic data which were analyzed in the 2-dimensional frequency domain. Initial processing of observed data consisted of spherical divergence corrections, wavelet shaping, predictive deconvolution using a special design and application window, filtering - followed by offset-dependent amplitude normalization with respect to forward modeled data to get a smooth, random amplitude spectrum sans the bubble pulse. Forward modeling is done via the central-difference scheme of Finite Difference method with the chief modeling parameters being the boundary conditions, time-domain damping parameter to prevent wraparound energy, appropriate quality factor and dispersion coefficient. Source and velocity inversion is done at selected frequencies using "efficient waveform inversion" to minimize the misfit of data residuals via the Gradient method. Inversion parameters (offset weighting, depth tapering, gradient wave-number filtering and masking) were tested and decided on a synthetic experiment where a stochastically generated model was used to generate real-time observed data. Although the inversion is stable and converges, leakage of velocity updates leads to the speculation about the adequacy of the source-receiver spacing at the data-acquisition stage. Initial velocity updates using OBS observed data are relatively small. The instrumental noise prior to the first-arrival picks is cosine-tapered before proceeding for further inversion – a scope for future work.

Keywords : TAG hydrothermal mound, efficient full waveform tomography, seismic data processing, stochastic modeling

Introduction

Waveform tomography is a computationally expensive but high resolution process to image the subsurface structure of the earth by an iterative inversion process that solves the full wave equation to find the model that best fits the observed data. This project deals with frequency domain, large offset, two-dimensional transmitted, acoustic refracted data from Ocean Bottom Seismometers (OBS).

Although ray theory or travel time tomography provides a very robust, stable solution to such imaging procedures, it is limited in resolution and reduces all the information contained in the experimentally acquired seismic waveforms to one travelttime pick.

While ray theory approaches can resolve up to $\sqrt{\lambda L}$ where λ is the wavelength in the medium and L the propagation distance, i.e. within the first Fresnel Zone, full waveform methods hope to achieve a resolution of λ provided full ray coverage is possible.

The crust is best characterized by the elastic equation, yet we used the acoustic approximation because s-waves would require finer discretization and 2-component data calculation thus increasing computational cost and also, picking first arrivals for S-waves is difficult so an initial travelttime model is difficult to obtain, especially in the presence of a rough topography. Frequency domain is used because it halves CPU time as inversions for only a few frequencies are required and once an impedance matrix is factorized, multiple source solutions are fast to calculate. By proceeding from low to high frequencies, low to high wavenumber coverage is obtained which mitigates the non-linearity of the inverse problem and attenuation and dispersion are easy to incorporate in the frequency domain.

Brief Theory

The 2D, frequency domain acoustic wave equation is given by [e.g. Aki and Richards, 1980] :-

$$\omega^2 \frac{P(x, z)}{K(x, z)} + \frac{\partial}{\partial x} \left[\frac{1}{\rho(x, z)} \frac{\partial P(x, z)}{\partial x} \right] + \frac{\partial}{\partial z} \left[\frac{1}{\rho(x, z)} \frac{\partial P(x, z)}{\partial z} \right] = -S(x, z) \quad \dots \text{Equation (1)}$$

where P = Pressure, ρ =density, K =bulk modulus, S =Source. The equation is solved using a central Finite Difference Scheme. The survey area is discretized into grid points and the value of the 3-by-3 matrix for each grid point is calculated and summed to form the (i,j) th element of the impedance matrix A . Since $i=1:N$ and $j=1:N$ where N is the number of grid-points, A has a dimension which is N^2 large, sparse, diagonally dominant (only $3N$ non-zero elements) and symmetric (source-receiver reciprocity). Thus, the differential full wave equation reduces to the form of $Ap=S$, where A =Impedance matrix, p =pressure and S =source. The forward and the inverse problems were solved using the softwares OMEGA and FULLWV developed by Dr. R.G. Pratt [e.g. Brenders and Pratt, 2007].

The inverse problem is solved iteratively to find the best fit model that would minimize the objective

function given by :-

$$E(m) = \frac{1}{2} \delta d^t \delta d^* \quad \dots \text{Equation (2)}$$

If we expand, by Taylor's series, the resultant change in the misfit function, also called the objective function, due to a delta change in model parameter is given by:

$$E(m + \delta m) = E(m) + \delta m^t \nabla_m E(m) + \frac{1}{2} \delta m^t H \delta m + O(\|\delta m\|^3)$$

On minimizing the misfit, the condition obtained is : $H \delta m = -\nabla_m E(m)$ where H is the Hessian matrix (i.e. the double derivative of the wavefield with respect to model parameters) and $\nabla_m E(m) = J$ is the Jacobian (i.e. the single derivative of the wavefield with respect to model parameters). The inverse of the hessian matrix can be interpreted as a smoothing filter over the Jacobian. Each i 'th column of the Jacobian is the partial derivative of the wavefield at all the grid points due to a perturbation of the i 'th model parameter. To efficiently solve for the Jacobian, we use the concept of virtual sources or the matrix F in the following equations.

$$J = \left[\frac{\partial u}{\partial m_1} \quad \frac{\partial u}{\partial m_2} \quad \dots \quad \frac{\partial u}{\partial m_n} \right] = S^{-1} [f^{(1)} \quad f^{(2)} \quad \dots \quad f^{(n)}] = S^{-1} F \quad \dots \text{Equation (3)}$$

where f is given by differentiating $Su=f$: $f^{(i)} = \frac{\partial S}{\partial m_i} u$

Putting the above approximations into the equation of the Gradient and assuming source-receiver reciprocity to hold, which means S^{-1} is symmetric, then :-

$$\begin{aligned} \nabla_m E(m) &= J^T \delta d = F^T [S^{-1}]^T \delta d \\ \nabla_m E(m) &= F^T v \\ v &= [S^{-1}]^T \delta d = [S^{-1}]^* \delta d \end{aligned} \quad \dots \text{Equation (4)}$$

Where v can be called a "backpropagated wave", which is a standard forward model with sources placed at receiver locations having magnitudes equal to data residuals at those receivers. In time domain, it is reverse-time convolution with the residuals. Essentially, any inhomogeneity on an otherwise homogenous medium acts as a scatterer when a plane wave passes over it causing it to create a scattered wavefield (the Jacobian) over and above the homogenous one. By Feynman's reciprocity principle, if the residuals or the scattered wave was backpropagated, it should plot back to its cause or the scatterer and hence image it. We followed the Gradient method for the inversion, which is outlined in Table 1.

Data Description

The data is acoustic, hydrophone data from 5 Ocean OBS deployed at the TAG hydrothermal mound at 26°N on the Mid-Atlantic Ridge (Figure 1). Travelttime tomography experiments [Canales et. al., in press] interpreted the mound to be located on a long-lived, normal, active fault as shown in Figure 1 (a). Data is aquired via WHOI-D2 OBS equipped with 3 component geophones and a hydrophone (Figure 1 (b)). The travelttime tomography model shown in Figure 2 is used as the starting model for waveform inversion. Our goal is to image small-scale features near the normal fault to give more information about fluid flow and tectonics of the area. The starting model has to be accurate enough to predict seismograms that match the observed seismograms to, at least, half a period. Otherwise, the inversion may cause the misfit function to converge at a local minimum and hence a wrong solution.

Data Processing

Data processing is an important step that improves the quality of the observations that are input into the inversion process. The steps followed are listed as follows:

- Multiples beyond an arrival time of 7.5s were muted.
- Spherical Divergence was corrected for using time-dependent correction = \sqrt{t}/V_0 , where V_0 depends on the value of velocity (=1500m/s in our case) at $t=0$.
- Noisy traces were edited
- Time reduced seismogram for velocity = 6km/s was used.

- Since any predictive deconvolution requires the source signature to be a minimum phase, the seismogram was wavelet-shaped as a response to a minimum-phase Butterworth wavelet of length 300ms and bandwidth = 2Hz to 45Hz.
- Predictive deconvolution operators were designed individually for each of the OBS gathers using a window of 1s around the first arrival far-offset, seismic refraction energy. Specifications are : Operator length = 90 points, predictive delay = 50 samples, bandwidth = 2Hz to 45Hz and 0.1% spectral whitening to make the Earth's response more random.
- Multiple mute is re-applied.
- The data is low-pass filtered using a Butterworth filter of length 51 points, a lower order of 3 and a higher order of 6 and bandwidth = 2Hz to 15Hz.
- Front-end noise, mostly instrument related, before the first arrivals are muted for a reduced time earlier than 1.75s
- The direct water wave in the receiver gathers is muted so that the inversion procedure specifically uses the large-offset, crustal refracted energy to fit the model.
- The data is resampled and a maximum modelled time of 10.5s considered for an input into inversion in the form of Shot Gathers.
- Offset-dependent scaling is done on the observed data in appropriate ratio with the forward modelled data on the Travelttime tomography model (Parameters and process described later).

Figure 3 compares the unprocessed and final seismogram for OBS gather 18, 61 shots, which looks visibly less noisier. The quality of the original data, however, looks worse than it is due to gain amplification of the display. Figure 4 is the receiver gathers of the seismogram after muting the direct water wave. Figure 5(a) shows the OBS gather for OBS 16 – 61 shots - in which the seismogram has been processed and filtered without wavelet shaping and deconvolution while 5(b) is the same gather which has been source signature corrected and deconvolved. Both 5(a) and 5(b) are compared with 5(c) which is the forward modelled seismogram for the OBS 16 gather using parameters described later and the travel-time tomography inverted velocity model. It can be seen in Figure 5(a), near shot 46, a distinct bubble pulse is seen interfering with the second arrival. Figure 5(b) removes the effect of this bubble pulse and makes the second arrival appear considerably clearer and coherent with the second arrival of the forward modelled seismogram in Figure 5(c). It is a positive sign to have these similarities in the seismograms to be compared even before the start of the inversion. Also 5(b) has more distinct waveforms at later arrival times as well compared to 5(b), which can be correlated to the arrivals of 5(c). Such examples can be seen in all the OBS gathers.

Figure 6 compares the amplitude spectra of the OBS 55 gather to cite another example of how the deconvolution step has improved the seismogram. 6(a) is the processed and filtered but undeconvolved seismogram while 6(b) includes wavelet shaping and deconvolution in the processing steps. The notch at frequency 10Hz has been removed considerably by the deconvolution, an important improvement as that frequency range encompasses the inversion frequencies and should have as much spectral content as possible for an efficient inversion. Figure 7 shows the spectra of all the OBS gathers before processing, after processing and after muting the direct wave. Evidently, removal of the direct wave has increased the flatness of the spectral content over the inversion frequencies range.

Amplitude Scaling

As seen in the Figure 5, there is considerable difference in the magnitude of the observed seismograms and the forward modelled seismogram. The former has to be scaled to the order of the latter so that

realistic data residuals can be backpropagated in the frequency domain. The steps undertaken are [Brenders and Pratt, 2007] :

- Input : Synthetic seismograms and observed seismograms, both with the direct wave muted.
- Natural logarithm of the RMS amplitude of each time trace calculated and plotted against offset (1 km binned), separately for observed and synthetic data.
- Equation of line that best fits $\log_e(\text{RMS_amplitude})$ vs. offset for offsets > 5 km. This is done to force the curve to fit the large-offset, crustal refracted energies instead of the components close to the direct wave.
- Correction factor for observed data =
$$\frac{\exp(mx + b)[\textit{Synthetic}]}{\exp(m1x + b1)[\textit{Observed}]} \quad \dots\text{Equation (5)}$$

where m,b and m1,b1 are calculated via a standard polynomial fitting algorithm for Synthetics and Observed data respectively. The values are extrapolated for offsets < 5km.

Forward Modelling Parameters

Forward Modelling is done using the travelttime tomography inverted velocity model (Figure 2). The density model was calculated from the velocity model using the velocity-density relationships of *Carlson & Raskin, 1984* and an attenuation model with Q=50 for velocities less than 6.5 km/s, Q=120 for velocities greater than 6.5km/s [e.g. Wilcock et. al. 1995] and a dispersion base frequency of 0.04Hz. The source used was a Keuper wavelet with a dominant frequency of 40 Hz, no delay and 2 excursions.

Considering a realistic crustal model, the maximum modelled frequency we are considering is 15Hz and the minimum velocity is that of water = 1500m/s. The minimum wavelength in the model is thus, 100m. We use 4 gridpoints per wavelength which makes our model gridsizes = 961 (x) by 321 (z) nodes for a survey area of 24km (x) by 8km (z). We used a maximum modeled time of 10.5s, a frequency sample of 0.95Hz and thus total of 112 frequencies.

Boundary Conditions

We tested two different boundary conditions : (1) Absorbing conditions on the lower 3 sides and free surface on the top and (2) Absorbing conditions for all the sides. For the former, there should be atleast 2-3 grid points between the source and the free surface as free surface literally implies P=0. In our experiment, the source is 10m (less than one point) away from the water surface, hence for the purpose of testing the best boundary conditions we modelled an extra 750m of water layer over the source. For the absorbing conditions, we incorporated sponge conditions (*Shin, 1995*) i.e. extra attenuation in the corners of the survey area box to make them more absorbing. Numerically, it introduces an extra damping matrix term on the left hand side of the acoustic wave equation and improves results significantly.

Figure 8 compares the difference in using the 2 different boundary conditions. Figure 8(a) shows a distinct second arrival at times after the direct wave which corresponds to the reflection off the top of the 750m water layer which reaches the OBS after the direct water wave. Other reflections are also evident. Figure 8(b) shows the absence of such reflections and a cleaner seismogram. We used this condition for our final modelling as we mute the direct wave, hence the presence or absence of reflections of the same do not make a difference as that component is muted out.

Time Damping Parameter

Inadequate sampling in the frequency domain leads to a time-wraparound problem i.e. the components occurring after the maximum modelled time wrap around T_{\max} and interfere with the components occurring before it. This can be prevented in the frequency domain by using complex frequencies.

$$\text{If } IFFT\{F(\omega)\} = \sum_{-\infty}^{\infty} f(t + nT_{\max})e^{-nT_{\max}/\tau}$$

$$\text{Then } IFFT\{F(\omega + i/\tau)\} = \sum_{-\infty}^{\infty} f(t + nT_{\max})e^{-n(t+nT_{\max})/\tau} \quad \dots\text{Equation (6)}$$

Multiplication of the time seismogram with $e^{-t/\tau}$ and setting $n=0$ would return the unaliased part. Therefore, all the components beyond T_{\max} are damped by a parameter τ and hence their wraparound is minimized. The method fails if the time series has non-zero values for negative times.

Figure 9(a) and 9(b) show the same OBS gather forward modelled using a damping constant τ of 0.5s and 3s respectively. The lower τ , i.e. the stronger damping, reduces wraparound significantly but causes unrealistic increase in energy arriving at later times after the direct wave (Shots 16-21). The higher τ , i.e. weaker damping fails to damp out a significant multiple, as seen at shots 51-61, but gives a much cleaner seismogram at later modelled times. To prevent the wraparound of the concerned multiple, the maximum modelled time was increased from 7.5s in Figures 9 (a) and (b) to 10.5s, which meant the number of modelled frequencies also increased from 112 to 157, causing the decrease of the Gibbs effect. Figure 9(c) shows the same OBS gather for the increased modelling time and it is evident that the seismogram remains less noisy and the wraparound is considerably avoided. Figure 10 compares the difference of damping parameters using free surface boundary conditions. As before, the prevention of wraparound of multiples is compensated by the increase of later-arrival, unrealistic energy.

Attenuation Modelling

In frequency domain, attenuation is incorporated by including frequency-dependent complex velocities. If $c(f)$ is the velocity of a point at frequency f , velocity c is given by :

$$c(f) = c \left[1 + \frac{1}{\pi Q} \ln \left(\frac{f}{f_0} \right) - \frac{i}{2Q} \right] \quad \dots\text{Equation (7)}$$

Dispersion is included to keep the propagation causal and f_0 is the base frequency at which no dispersion occurs and Q is the quality factor. (Aki & Richards, 1980)

Spatial attenuation was included because the rate of slope of the observed binned RMS data falls more steeply than for the forward modelled data. Approximate values from the off-axis inversion at the East Pacific Rise (Wilcock et al, 1995) were considered and values of Q were spatially allotted to the grid points depending on the velocity model. The Q -model that gave the least misfit between the forward and observed time-series-RMS vs. offset was adopted. Misfit was calculated using the root-mean square value from all offsets between the two graphs (red and green) in Figure 11 divided by the maximum misfit. Figure 11 (a) shows the time-series-RMS vs offset of the forward modelled synthetics compared to the observed seismograms for a modelling experiment without attenuation. The misfit

between the two graphs is not only visibly apparent but also numerically high (4.25e-2 – compare to a maximum amplitude of 14e-5). Figure 11 (b) shows the same graphs for a forward modelling experiment in which an attenuation model of Q=50 for velocities greater than 6.5km/s and Q=120 for velocities less than 6.5km/s. The fit is visibly better and the misfit is 4.3833e-3 – compare to a maximum amplitude of 6e-4. This attenuation model was then used for the inversion.

Efficient Waveform Tomography

It is important that the correct inversion frequencies be chosen so that a full wavenumber coverage is obtained, specially at the lower frequencies in order to mitigate the non-linearity of the inverse problem. For the maximum or any frequency f , the maximum and minimum wavenumber, k , inverted for is given by :-

$$k_{z-\min} = \frac{2f\alpha_{\min}}{c_0} \quad \text{and} \quad k_{z-\max} = \frac{2f}{c_0} \quad \dots\text{Equation (8)}$$

For continuous wavenumber coverage, the maximum k inverted at one frequency has to match the minimum k inverted for at the next frequency. This condition for the next inversion frequency can be expressed as :-

$$f_{n+1} = \frac{f_n}{\alpha_{\min}} \quad \dots\text{Equation (9)}$$

Sirgue & Pratt, 2004

By the formula, the inversion frequencies within 2Hz and 15Hz are : 2.0000, 3.6056, 6.5000, 11.7180. However, in order to increase data redundancy in the wavenumber domain, we inverted for 7 frequencies : 2.0, 3.5, 5.0, 6.5, 9.0, 11.5, 15.0. In Figure 12, the blue vertical lines show the adequate wavenumber coverage for the calculated inversion frequencies in the form of a step-like pattern in the f - k domain. The inversion frequencies used are indicated by the thick green lines which overlap in the k -domain that is to increase the overlap of the inverted wavenumbers.

Inversion

Using SI units for length and frequency cause the objective function to be of the order of 1e-15 which almost equals the minimum floating point number. Iterative schemes work on reduction of the error/misfit and hence, numerical instability arises at such low values.

Before inversion, thus, distances are scaled down (i.e. 12000m => 12km), frequencies are scaled up (i.e. 2Hz => 2000mHz) and Time is scaled down (i.e. 10ms => 0.01s OR 10.5s => 0.0105 ks). Resultantly, as verified by equation for $A_p=S$, A is uniformly scaled down by 1e+6, hence u and consequently misfit objective function scales up by 1e+6, improving the stability.

A source inversion has to be done at each frequency before proceeding to a velocity inversion. : If the wave-equation in matrix form is $Sp=of$ where f = a priori source estimate, then the inverted source is “of”

$$\text{where } o = \frac{p_o^T d^*}{p_o^T p_o} = \frac{\sum_{i=1}^N p_{oi} d_i^*}{\sum_{i=1}^N p_{oi} p_{oi}^*} \quad \dots\text{Equation (10)}$$

O is a least squares estimate calculated by summing over N , d =data and p_o =wavefield calculated with f as source. The assumption for this inversion is that the initial velocity model is almost accurate, i.e. if the

source had been known then the model would predict the observed data almost exactly. The extracted source usually lags the desired one used in deconvolution (especially if the undeconvolved wavelet is not minimum-phase), hence an appropriate advance is required at every frequency inverted for. (Pratt, 1999)

For each of the 7 frequencies inverted for sequentially, the monochromatic component of the direct waterwave-muted observed data was extracted. A background velocity model of 4km/s and appropriately calculated density and attenuation models were used to calculate a background forward wave which is subtracted from the forward model solution at every iteration, and the difference used to compute the data residuals. This focuses the updates to the the velocity model over and above the background velocity and wavenumber. It is also instrumental in considerably removing the direct water wave from the forward model which is important because the direct wave in the observed seismograms is muted after processing, so data residuals are more realistic if the same is implemented for the forward synthetics as well. (Hicks & Pratt, 2001)

20 iterations per frequency were used and the iterations were stopped if the inversion failed to reduce the misfit function with respect to the previous iteration. An offset weighting filter was used (7km-8km-20km-30km) and the data residuals were tapered off for offsets less than 8 km. A depth filter (0-0-6km-6.5km) was used to taper the gradient below certain depths. An important parameter was the application of a low-pass wavenumber filter which forced the inversion to invert only for a particular range of wavenumbers for each frequency. Starting with $\lambda_{\min}(x) = 5\text{km}$ and $\lambda_{\min}(z) = 1\text{km}$ at 2Hz, the wavenumbers passed are increased to $(x) = 1\text{km}$ and $\lambda_{\min}(z) = 50\text{m}$ at 15Hz. This constraint keeps the problem as linear as possible. All values of the gradient above the sea-floor topography was set to zero.

Results

Figure 13(a) shows the inversion results at each frequency using OBS. The traveltimes model is subtracted from velocity model inverted at each frequency to highlight the update. Figure 13(b) shows the product of the gradient and steplength at each frequency. As expected, the maximum update occurs at 6.5Hz because it is the first frequency with high spectral content (Figure 8). The lower frequencies are inverted to avoid non-linearity without much change – waveform tomography should never change the long wavelengths in the model as it amounts to changing the background velocity. Figure 14 shows the objective function plotted for the last iteration vs frequency, normalized to the maximum value. Percentage reduction per frequency of the objective function plotted. Convergence is reached when no more reduction occurs. In the absence of gradient filtering, offset weighting cause unrealistically small λ updates at lowest frequencies and absence of water-gradient mask cause velocities of water to increase by 500-600m/s as shown in Figure 15(a). Absence of scaling mostly caused the data residuals to be 'considered' equal to zero, hence no back-propagated wave was identified, or the inversion iterated 1-2 times giving unrealistic updates (Figure 15(b)). Thus, although no small scale features were inverted, parameters have been well selected to keep the model stable throughout the independent frequency inversions.

Figure 16(a) shows an overlay of the forward model synthetics performed on the traveltimes tomography model and the processed observed data (receiver gather, 61 shots, for OBS 17). By visible interpretation, it seems that although the direct wave first arrival matches, the seismic energy for the observed data is delayed. However, closer inspection (Figure 16(b)) shows that the energy before the interpreted first arrival of the observed seismogram has amplitudes as low as the instrument/experimental noise - but it is

coherent through all the shots, which makes this arrival the true first arrival. The first arrival picks from the travel-time tomography experiment were used to make a cosine taper to damp the noise before the picks for all OBS, all shots. Figure 16(c) shows an individual traces from OBS 55, Shot 60 for the forward modelled trace, the observed OBS trace and the noise-damped observed OBS trace. Although the former has Gibbs effects, the noise-damped trace and the forward model trace seems to match within a period. Appropriate selection of inversion parameters could give better results *if* the ray coverage and OBS/shot spacing is adequate at the data acquisition stage.

Stochastic Modelling

To check the adequacy of the OBS and shot spacing in inverting for a large velocity model in such a complex geologic setting, we constructed a realistic synthetic velocity model using stochastic perturbation on the Travel Time tomography model. Velocity perturbations are considered a stochastic process described by a set of observable statistics. The amplitude spectrum was calculated in wavenumber domain by the following Formula :

$$P(k) = \frac{4\pi a_x a_z}{G_v(0)(1+k^2)^{(1+\nu)}} \quad \text{where } k = \sqrt{k_x^2 a_x^2 + k_z^2 a_z^2} \quad \dots \text{Equation (11)}$$

$G(0)$ is related to Bessel function(2nd kind, order ν) = 0.2

ν = Hurst number = 1.5

a_x = horizontal characteristic length = 1km

a_z = vertical characteristic length = 200m

The phase is randomly generated and stochastic constants are adjusted till perturbation of desired value is obtained (*Pullammanappallil et al, 1997*). To avoid horizontal symmetry, a grid double the size required was considered and one half chosen. Perturbations above sea-floor topography were masked. Figure 17 shows the perturbation model and final synthetic velocity model.

The synthetic stochastic model is forward modeled for 0-20Hz using a Keuper wavelet of dominant frequency = 40Hz. This synthetic seismogram is used as the observed dataset. It is compared to the forward modelled data to assess the feasibility of the Waveform inversion. Figure 18 shows 2 such individual traces where the first arrival both the seismograms matches within a period quite well, indicating that the TT model is suitable to use as a starting one. Ideally, this model should give good results, provided acquisition sampling and parameters are sufficient.

We tested an inversion scheme using the same parameters as those used in the Observed TAG Dataset. The inversion diverged after the first two inversion frequencies if the wavenumber filter was not restrictive enough. If a strong filter (filtering out all wavelengths lower than 2 km in depth – judging by the wavelength of the perturbations) was used, the inversion converged giving results shown in Figure 19. However, comparing Figure 19 and Figure 17(b), it is evident that although the inversion has lowered the velocity of the upper crust at a depth of 4.75 km but these do not match the perturbation model in terms of spatial location. Comparison of the synthetic seismogram on the true stochastic model and the forward modelled seismogram on the updated model (via inversion) shows that the update is causing the first arrival traveltimes to get delayed, as they should, but at the cost of an update in the wrong spatial location. It leads us to interpret that there can be occurring, a case of leakage of the updates due to insufficient OBS or shot sampling. Seismic waveform tomography is an extremely new field in

Exploration seismology, initialized only in the last decade, hence there is a lot yet to be discovered with respect to the acquisition geometries and parameters. Considerable work would have to be done to re-model inversion parameters and tested on this synthetic model to counter the effect of spatial undersampling at the acquisition stage, only then can dependable results be expected from the Observed data.

Acknowledgements

I would like to extend my gratitude to Dr. Robert A. Sohn and Dr. Daniel Lizarralde for very helpful discussions and sharing with us, their valuable suggestions.

References

- K. Aki and P.G Richards, Quantitative Seismology, theory and methods, *W.H. Freeman and Co*, 1980.
- A.J. Benders and R.G. Pratt, Full waveform tomography for lithospheric imaging : results from a blind test in a realistic crustal model, *Geophys.J. Int.*, 168, 133-151, 2007.
- A.J. Benders and R.G. Pratt, Efficient waveform tomography for lithospheric imaging : implications for realistic, two-dimensional acquisition geometries and low-frequency data, *Geophys.J. Int.*, 168, 152-170, 2007.
- J.P. Canales et al., Crustal structure of the Trans-Atlantic Geotraverse (TAG) segment (Mid-Atlantic Ridge, 26° 10'N): Implications for the nature of hydrothermal circulation and detachment faulting at slow spreading ridges, *Geochem. Geophys. Geosyst.*, doi:10.1029/2007GC001629, in press.
- G.L. Christeson et al., The shallow attenuation structure of the fast-spreading East Pacific Rise near 9°30'N, *Geophys. Res. Lett.*, 21, 321-324, 1994.
- B.J. deMartin et al., Kinematics and geometry of active detachment faulting beneath the Trans-Atlantic Geotraverse (TAG) hydrothermal field on the Mid-Atlantic Ridge, *Geology*, 35, 711-714, 2007.
- G.J. Hicks and R.G. Pratt, Reflection Waveform inversion using local descent methods : estimating attenuation and velocity over a gas-sand deposit, *Geophysics*, 66, 598-612, 2001.
- G. Nolet, Seismic Tomography, *D. Reidel publishing Company*, 301-322, 1987.
- S. Operto et al., Crustal seismic imaging from multifold ocean bottom seismometer data by frequency domain full waveform tomography : Application to the eastern Nankai trough, *Journal of Geophysical Research*, Vol. 111, B09306, 10.1029/2005JB003835, 2006.
- R.G. Pratt and M. H. Worthington, Inverse theory applied to multi-source cross-hole tomography, Part I : Acoustic wave equation method, *Geophysical Prospecting* 38, 287-310, 1990.
- R.G. Pratt et. al. Gauss Newton and full methods in frequency-space seismic waveform inversion, *Geophys.J. Int.*, 133, 341-362, 1998.
- R.G. Pratt, Seismic waveform inversion in the frequency domain, Part I : Theory and verification in a physical scale model, *Geophysics*, 64, 888-901, 1999.
- R.G. Pratt and R.M. Shipp, Seismic waveform Inversion in frequency domain II : Fault delineation in sediments using crosshole data, *Geophysics* 1998.
- S. Pullammanappallil et. al., Estimation of crustal stochastic parameters from seismic exploration data, *Journal of Geophysical Research*, 100, B7, 15269-15286, 1997.

C. Revaut et. al., Multiscale imaging of complex structures from multifold wide-aperture seismic data by frequency-domain full-waveform tomography : application to a thrust belt, *Geophys. J. Int.*, 159, 1032-1056, 2004.

Changsoo Shin, Sponge boundary condition for frequency-domain modeling, *Geophysics*, 60, 1870-1874, 1995.

Changsoo Shin et. al., Efficient calculaion of a partial-derivative wavefield using reciprocity for seismic imaging and inversion, *Geophysics*, 66, 1856-1863, 2001.

A. Tranatola, Inversion of seismic reflection data in acoustic approximation, *Geophysics*, 49, 1259-1266, 1984.

L. Sirgue and R.G. Pratt, Efficient waveform inversion and imaging : a strategy for selecting temporal frequencies, *Geophysics*, 69, 231-248, 2004.

Y. Wang and Y. Rao, Crosshole seismic waveform tomography – I. Strategy for real data application, *Geophy. J. Int.*, 166, 1224-1236, 2006.

W.S.D. Wilcock et. al., Seismic attenuation structure of the East Pacific Rise near 9°30'N, *Journal of Geophysical Research*, 100, B12, 24147-24165, 1995.

Oz. Yilmaz, Seismic Data Analysis, Volume 1 and 2, *Society of Exploration Geophysicists*, 2001.

T. Yokota and J. Matsushima, seismic waveform tomography in the frequency-space domain : selection of the optimal temporal frequency for inversion, *Exploration geophysics*, 35, 19-24, 2004.

Figures and Tables

1) $\mathbf{u} = \mathbf{S}^{-1} \mathbf{f}$	Compute the forward-propagated wavefield.
2) $\mathbf{v} = [\mathbf{S}^{-1}]^t \delta \hat{\mathbf{d}}^*$	Back-propagate the data residuals.
3) $g_i = \mathcal{R}e\{\mathbf{u}^t [\frac{\partial \mathbf{S}^t}{\partial p_i}] \mathbf{v}\}$	Calculate the gradient direction.
4) $\mathbf{c} = \mathbf{B} \mathbf{g}$	Form the preconditioned gradient direction.
5) $\delta \mathbf{p}_{(k)} = \mathbf{c} - \gamma \delta \mathbf{p}_{(k-1)}$	Form the conjugate gradient direction.
6) Estimate optimum α	Perform a line search for the step-length α .
7) $\mathbf{p}_{(k+1)} = \mathbf{p}_{(k)} - \alpha \delta \mathbf{p}_{(k)}$	Update the model.

Table 1 : Gradient method scheme followed for the inversion process. The Hessian matrix was approximated via a Conjugate gradient serach and a line-search method. If the Hessian is partially or fully calculated, the methods used are Gauss-Newton or Full-Newton methods respectively.

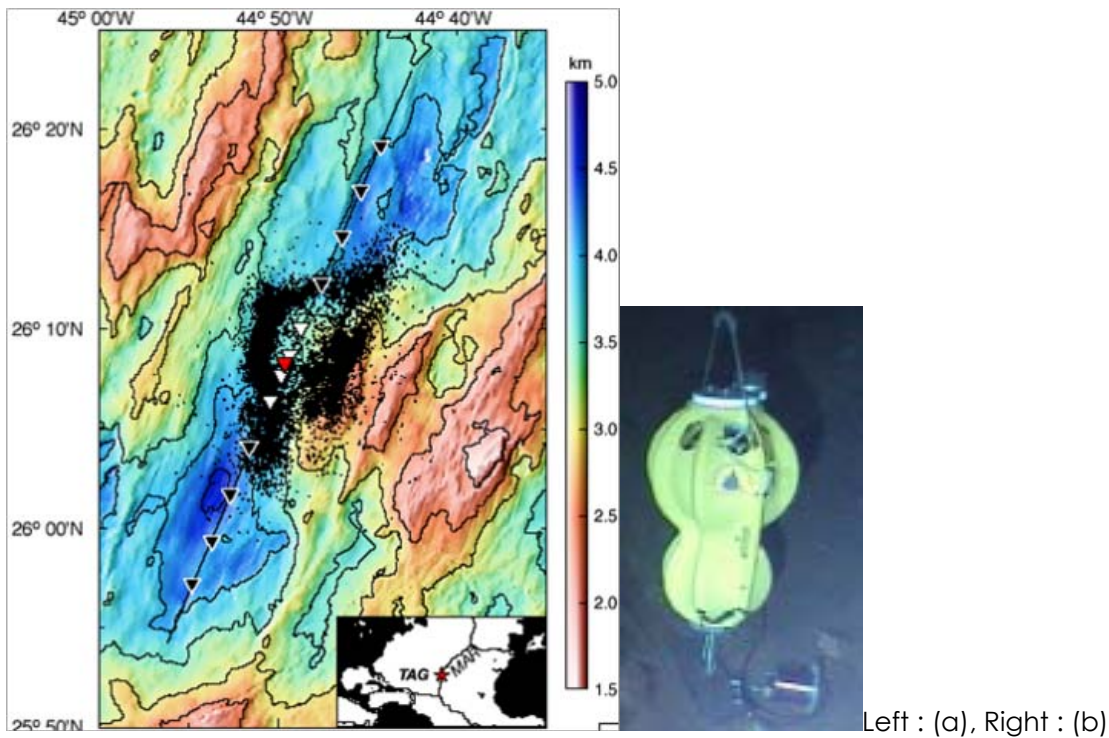


Figure 1(a): The bathymetric map of the area of Data collection. The red triangle indicates the TAG hydrothermal mound, the white triangles are short period OBS with geophones and hydrophones, the black triangles are long period OBS with only geophones. In the Waveform Tomography experiment, we used data from the 5 OBS shown as white triangles to image the Hydrothermal section of the TAG. The black dots are the microearthquakes which are interpreted to be the trace of the normal fault. (b) Photograph of an OBS.

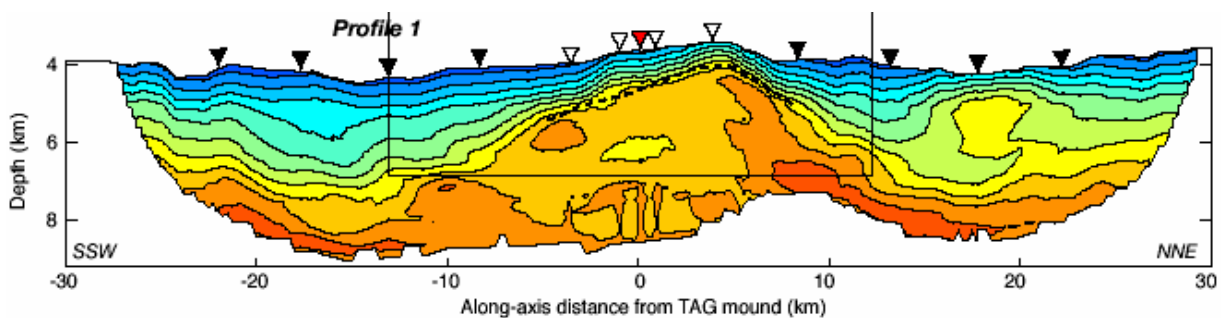


Figure 2 : Traveltime Tomography inverted velocity model (Canales et al,2007). The dotted line shows the interpreted normal fault and the red triangle is the location of the TAG hydrothermal mound on the hanging wall of this fault.

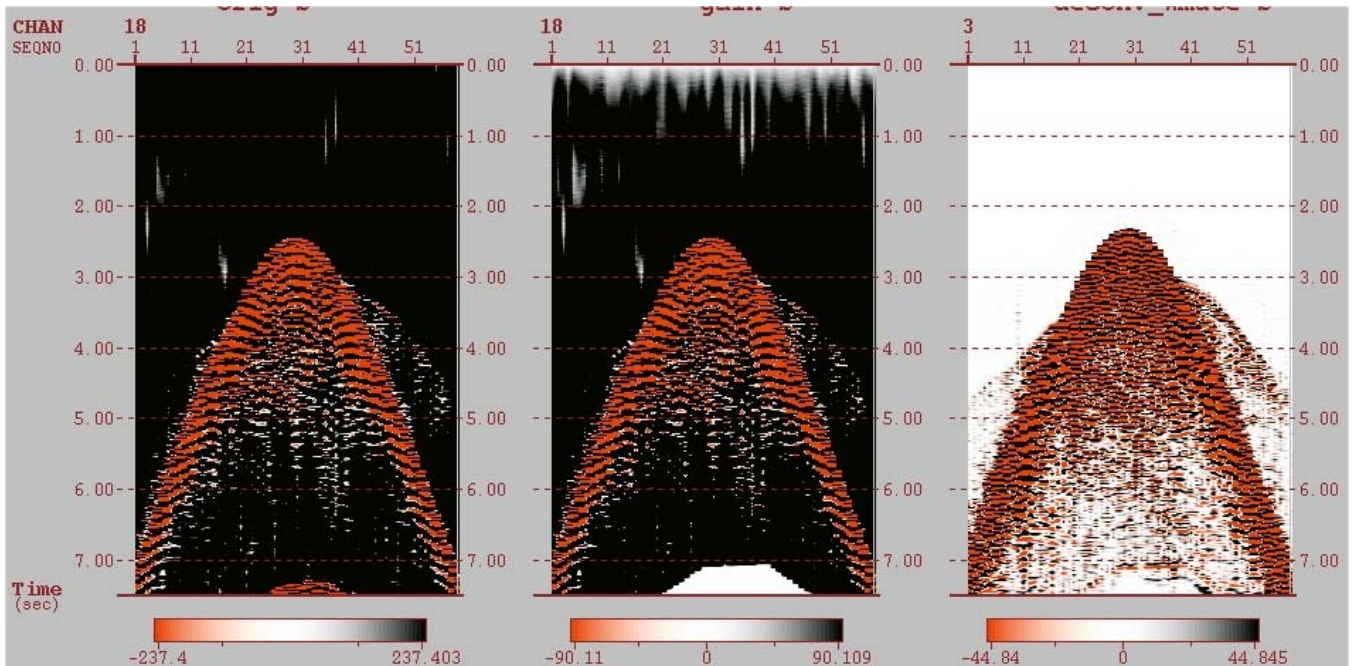


Figure 3(a) Unprocessed Data. (b) Gain Corrected, back end multiple muted data. (c) Wavelet shaped, deconvolved, filtered data with Mutes. Data for OBS18, 61 shots.

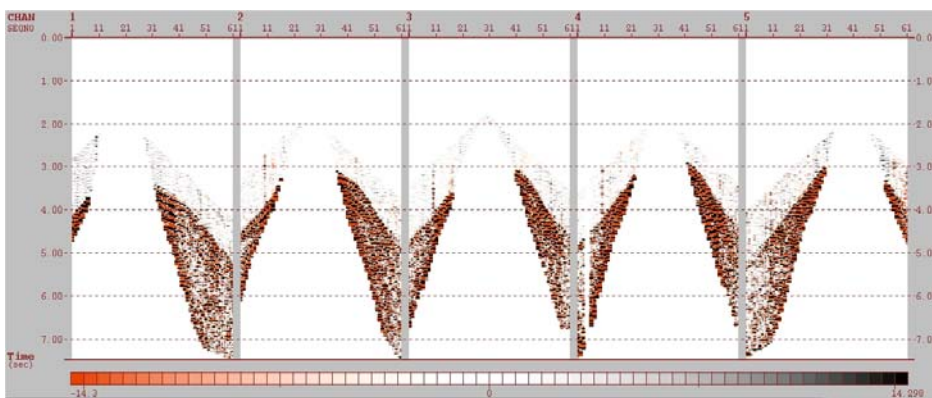
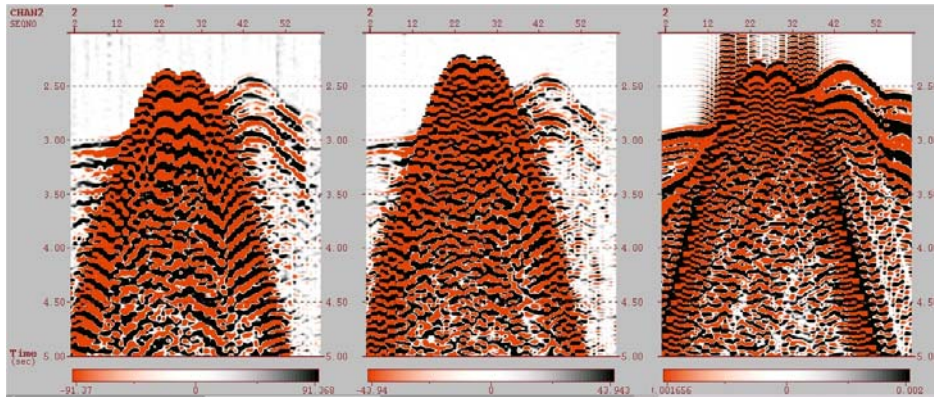


Figure 4 : Final Processed data to input to Inversion. (Left to right: OBS 55,16,18,17,32. They are sorted according to the location from Left to Right on the FDM grid)

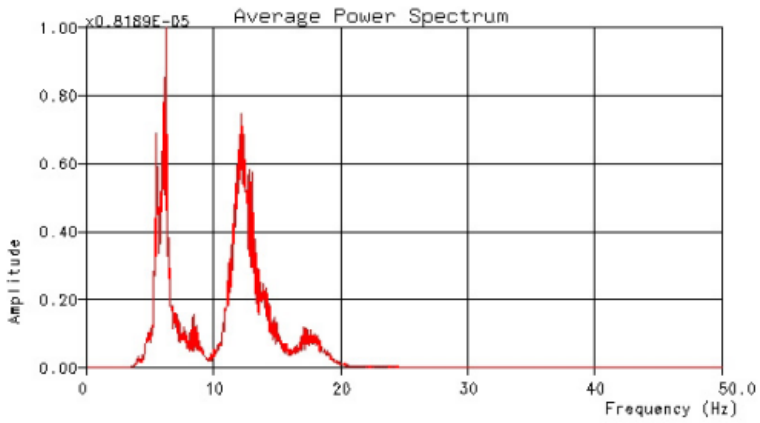


(a)

(b)

(c)

Figure 5 : Comparison of the forward modeled data and processed observed data for OBS 16, 61 shots. (a) Undeconvolved but processed data. (b) Processed, deconvolved data (c) Forward modeled data. The bubble pulse which interferes with the second arrival in the Observed seismogram is considerably removed by deconvolution. This second arrival now correlates with the second arrival of the synthetic seismogram. Deconvolution makes the arrivals more distinct.



CHAN 55 SEQNO 1 T1= 0 T2= 19990
 SEQNO 61 T1= 0 T2= 19990

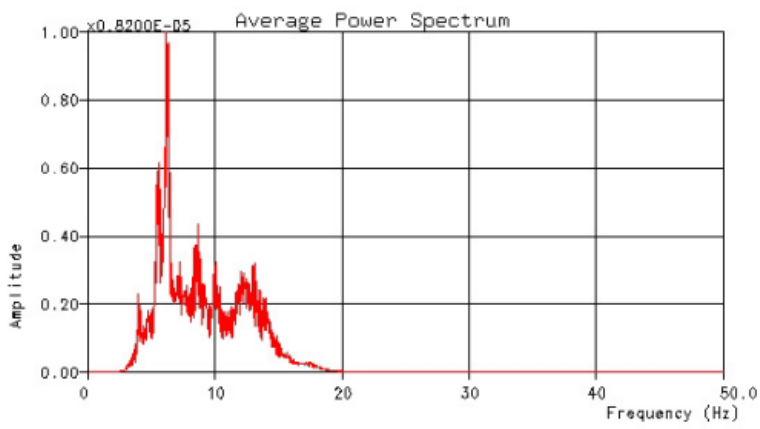


Figure 6 : Amplitude Spectrum of observed seismogram of OBS55 before (top) and after(bottom) deconvolution, all other parameters remaining the same. The notch in the energy level at 10Hz (a dominant component in the inversion frequency spectrum) is considerably reduced due to deconvolution.

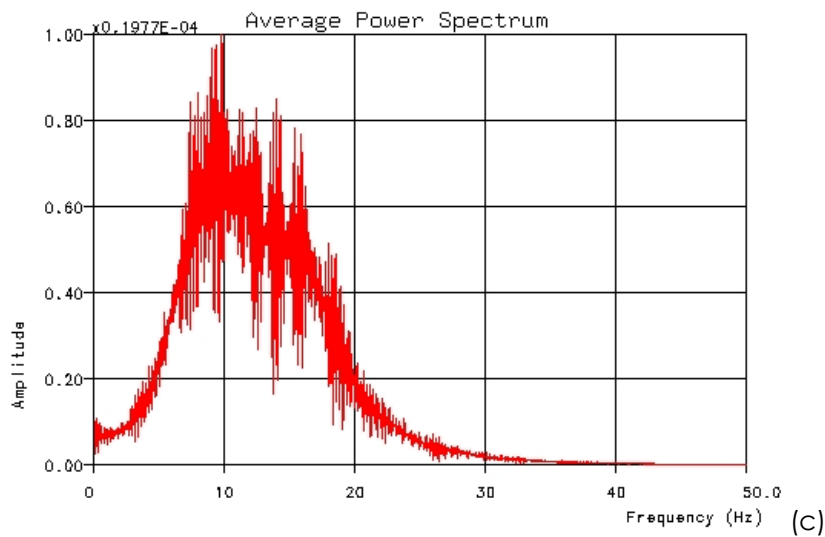
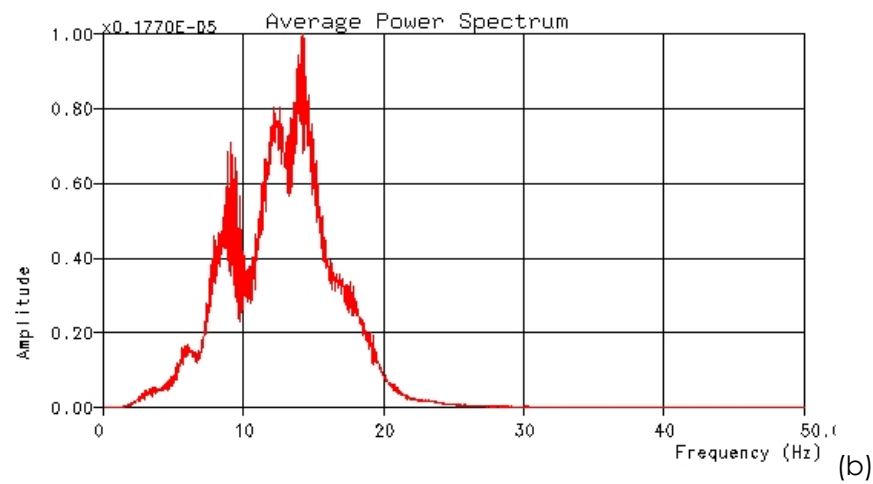
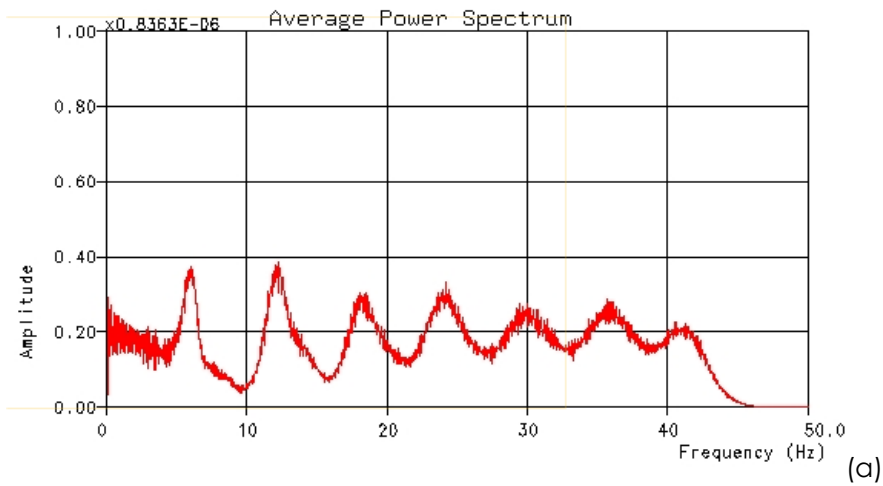


Figure 7(a) : Amplitude Spectrum of the unprocessed Data. (b) : Amplitude Spectrum of the Final Processed and deconvolved Data (c) : Amplitude Spectrum of the Seismogram of (b) with the direct

water wave muted. The inversion frequency range, after processing, contains uniform distribution of seismic energy as opposed to undulating notches in the unprocessed data.

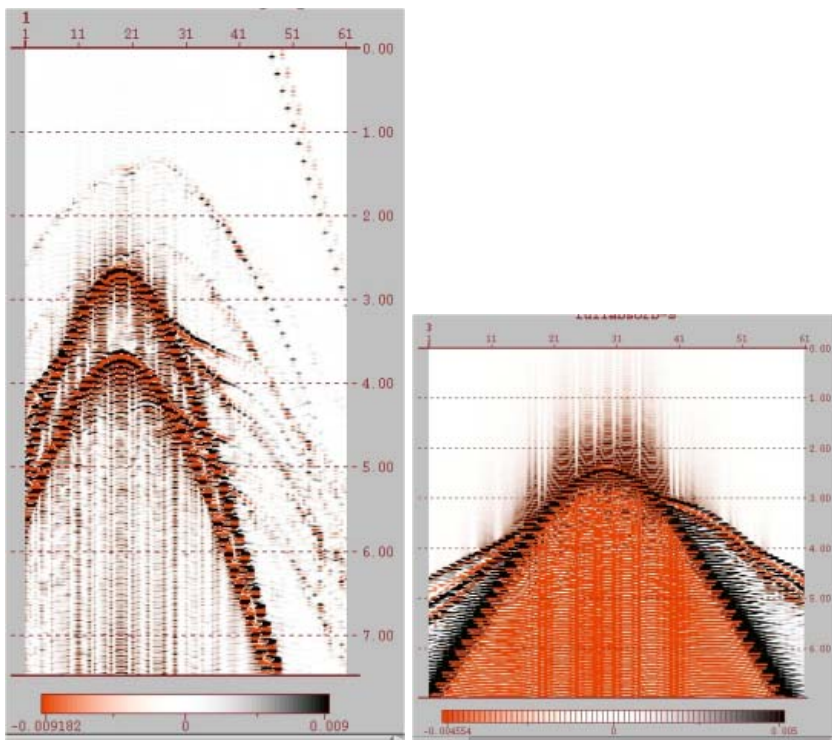
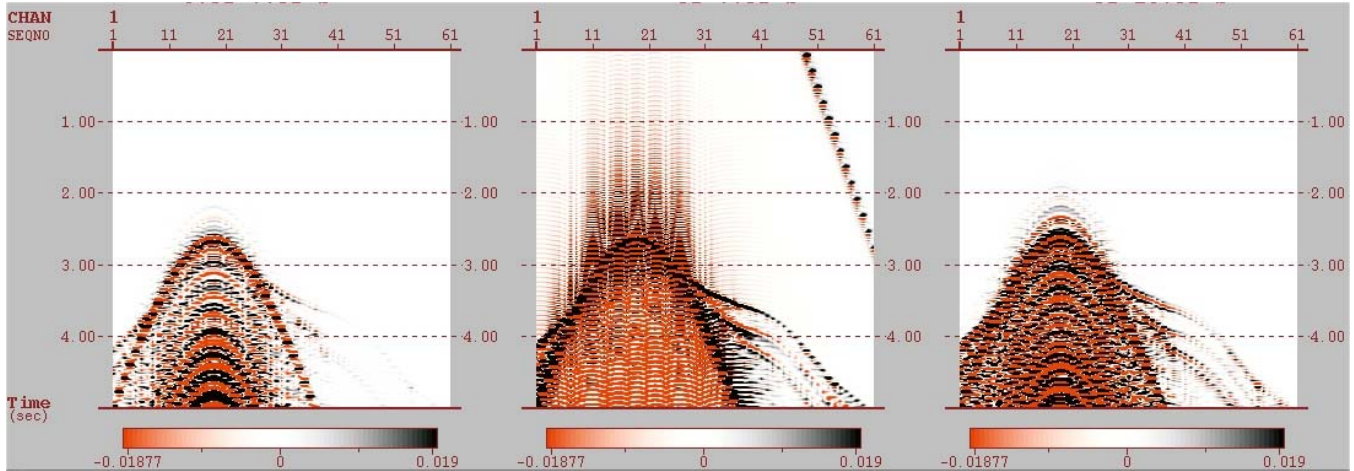


Figure 8(a) : Synthetic forward modeled seismogram for OBS 55 gather in which free Surface is included ($\tau=3s$, 750m water layer above the source). (b) modeled seismogram for OBS 55 gather in which all sides have absorbing boundaries ($\tau=3s$). Modeled time = 0 to 7.5s and both have sponge conditions included. The free surface condition introduces a distinct reflected direct wave off the top of the water layer. Although, in the experiment, sources were places 10m below the sea surface, the extra 740m of water layer was added to compute the synthetics to bring out the reflected wave distinctly separated from the direct arrival.

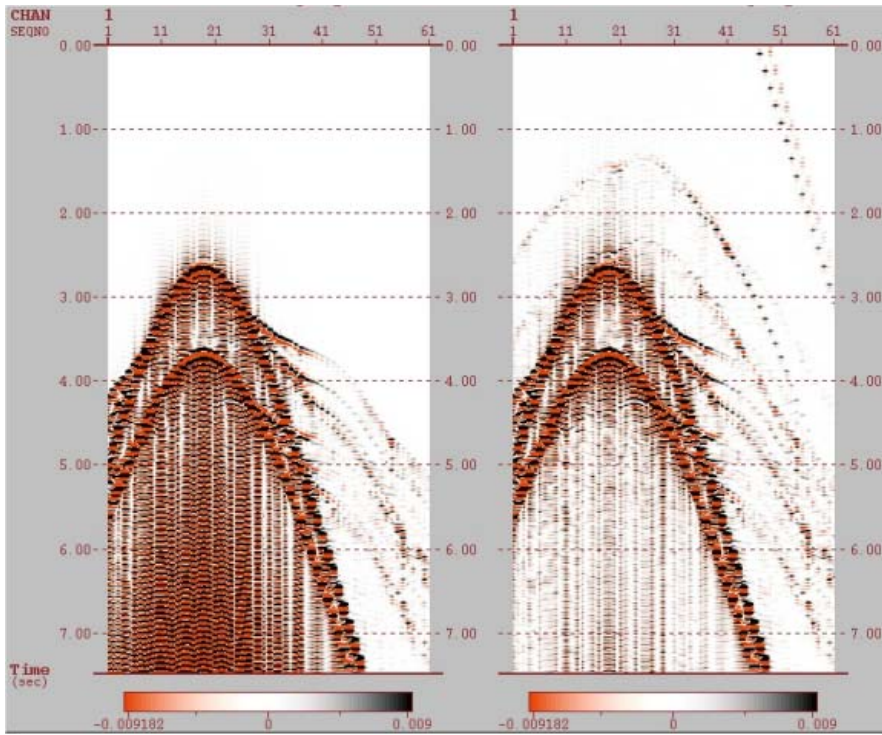


(a)

(b)

(c)

Figure 9(a) : Synthetic seismograms of the OBS Gather 55, modeled for damping constant 0.5s, maximum modeled time of 7.5s and 112 frequencies. Unrealistically high amounts of energy arriving at later times render this model undependable (b) Synthetic seismogram for Same OBS Gather 55, modeled for damping constant = 3s, all other parameters remaining the same. A distinct wraparound of energy arriving till 3s after the maximum modeled time of 7.5s is seen. (c) seismograms of the OBS Gather 55 for max. Time = 10.5s, 157 frequencies, damping=3s. Modeling more frequencies and longer times decreases aliasing to a great extent too. A suitable value of damping and modeled time reduces wraparound *and* yields realistic synthetics. No attenuation model included and Full absorbing boundary conditions are used.



(a)

(b)

Figure 10(a) : Synthetic forward modeled seismograms for OBS 55 using damping parameter = 0.5s, $T_{max} = 7.5s$ and 112 frequencies. Top surface is a free surface condition. (b) Same as (a) except that the damping constant is 3s. Similar effects as those in Figure 9 are observed, that is, although a lower damping value fails to suppress the wraparound, it yields a cleaner seismogram.

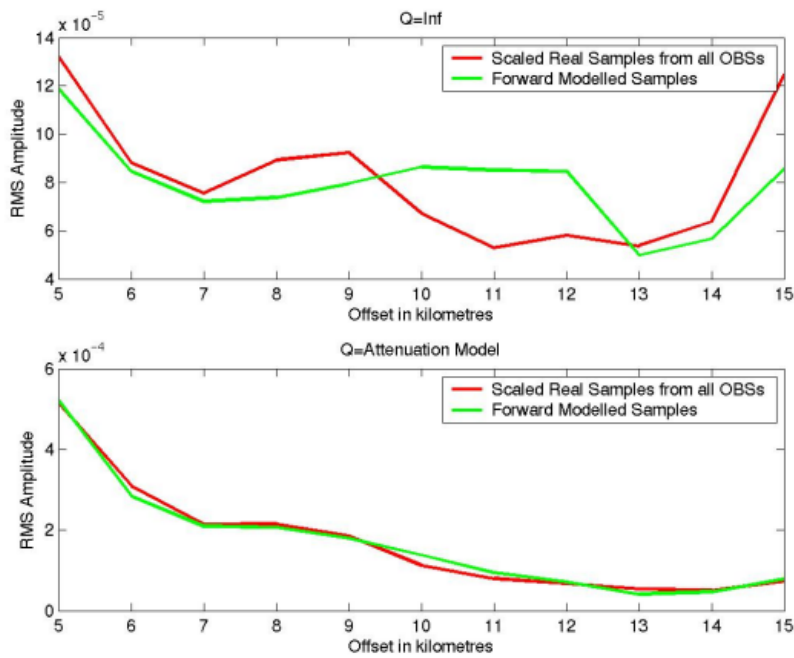


Figure 11 : Comparison of RMS amplitudes of the Observed Data and Forward Modeled Data vs. 1km offset bins. Top figure: Q=Infinite or no attenuation. Bottom Figure: Q=50 for $V < 6.5 \text{ km/s}$ and Q=120 for $V > 6.5 \text{ km/s}$. Misfit is mathematically defined as the root mean square average of the difference between Forward modeled samples and scaled observed samples over all offsets, normalized to their highest values. Use of an attenuation model not only gives a visible better fit but also improves the mathematical misfit by one order.

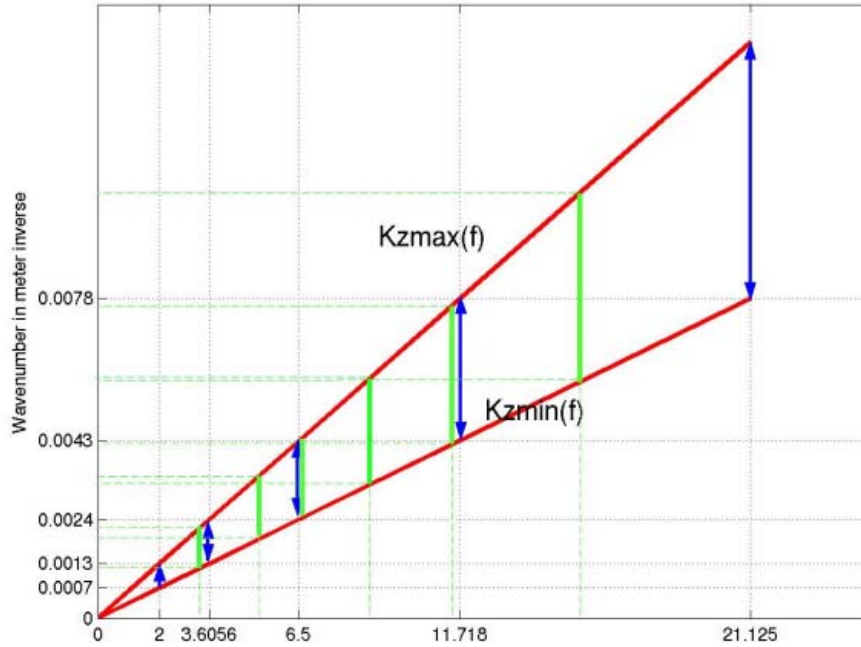


Figure 12 : The wavenumber-frequency space for the geometry of our experiment. The enclosed space within red lines indicate the of wavenumber coverage for each frequency. The vertical blue lines are the k-coverage for each of the minimum number of frequencies that should be inverted (calculated by Equation 9 and ticked on the X-axis) and the vertical green lines are the k-coverage of the frequencies actually inverted for. As seen, there is data redundancy on the k-space, to increase the stability of inversion.

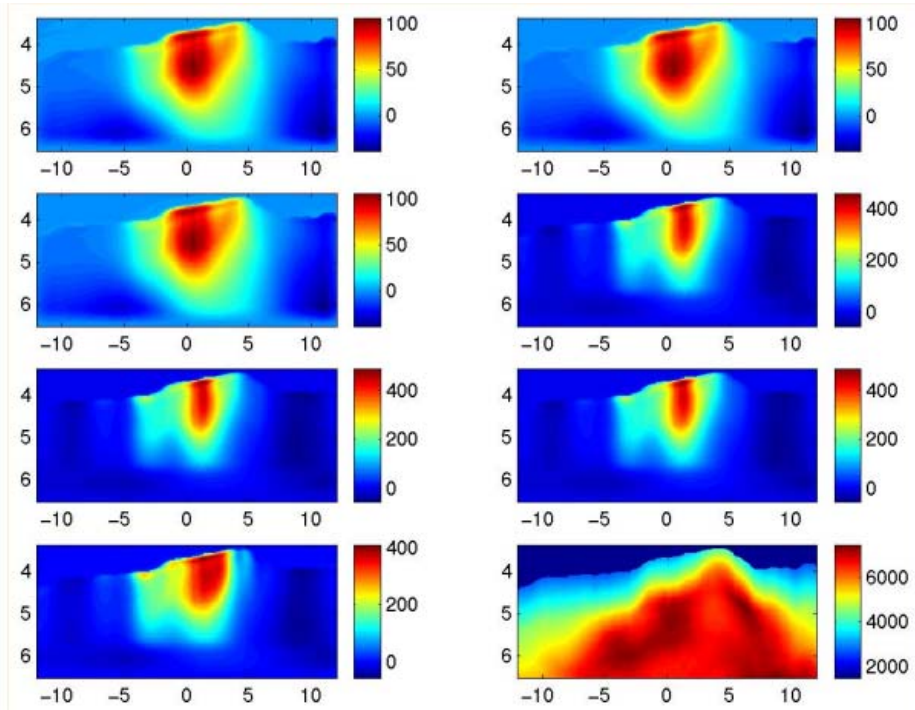


Figure 13(a) : The velocity model at each frequency minus the starting model, to show the updates with respect to the original at each sequential stage. As expected, the maximum update occurred at 6.5Hz as the first spurt of seismic energy on the spectrum arrives just after 5Hz. All colors indicate velocity marked in m/s. Both axes are marked in km.

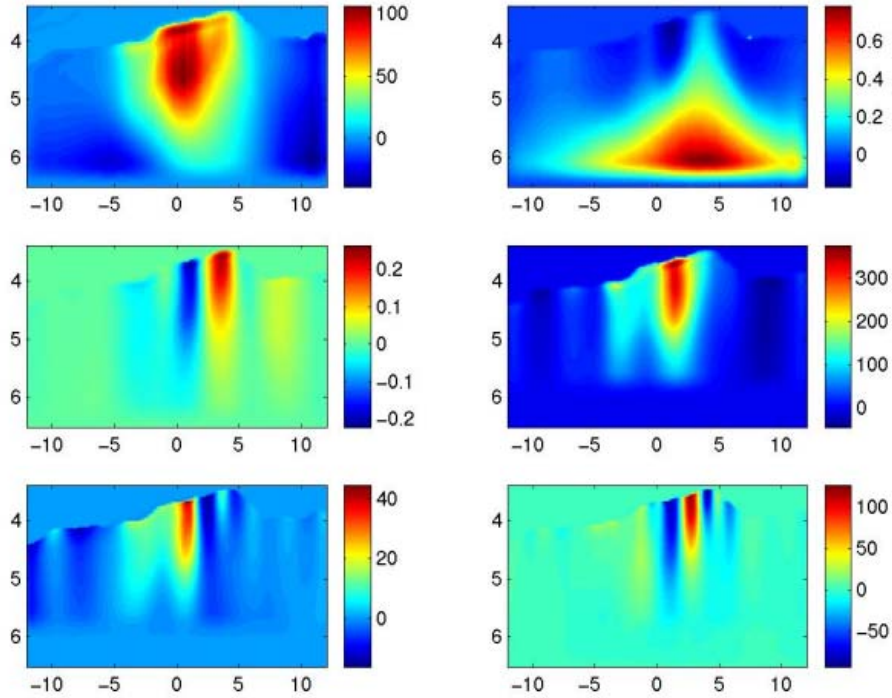


Figure 13(b) : The velocity model at each frequency, labeled, minus the inverted model at the previous frequency, to show the update at each sequential stage. Since it is dependent on the gradient, this update can be thought of as the product of the Gradient and the conjugate step-length. All colors indicate velocity marked in m/s. Both axes are marked in km.

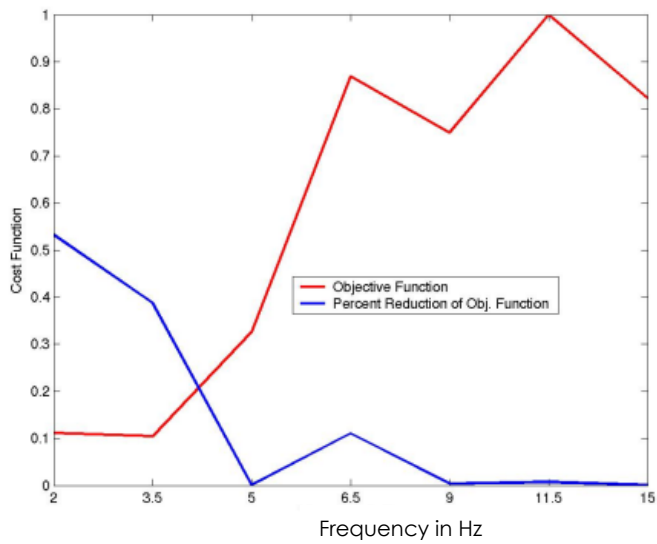


Figure 14 : Plot of the misfit function and percent reduction of the misfit vs. inversion frequencies. At any inversion frequency, if the update to the velocity model does not successfully reduce the misfit function as compared to the previous iteration, the iterations are said to be divergent and they are stopped. With frequency, this percentage reduction decreases as is seen in the graph.

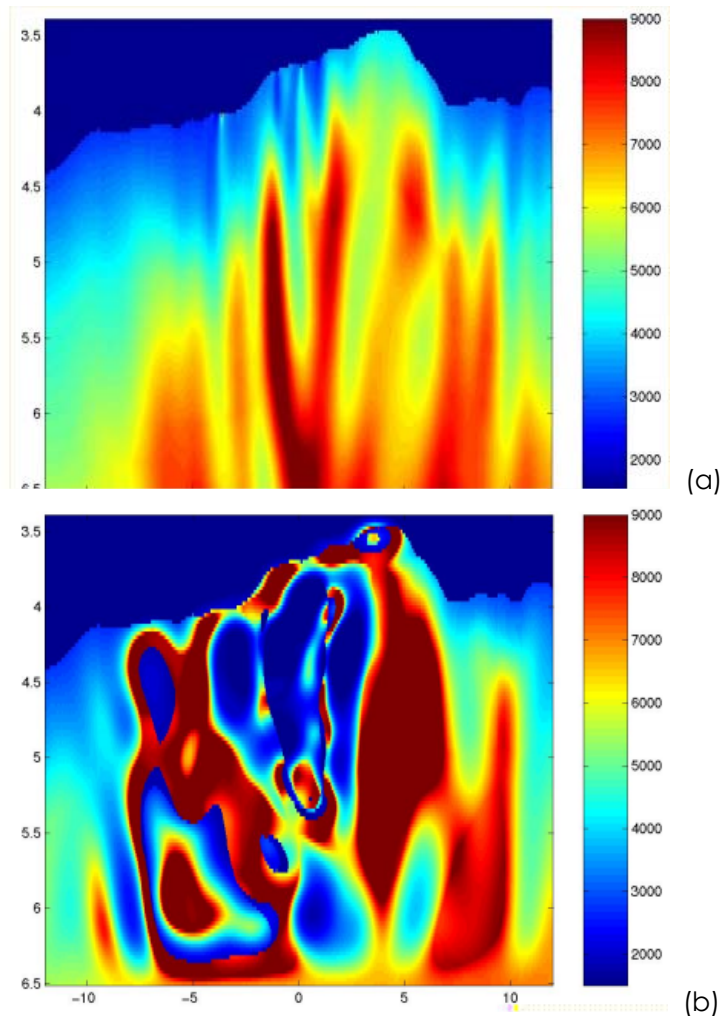
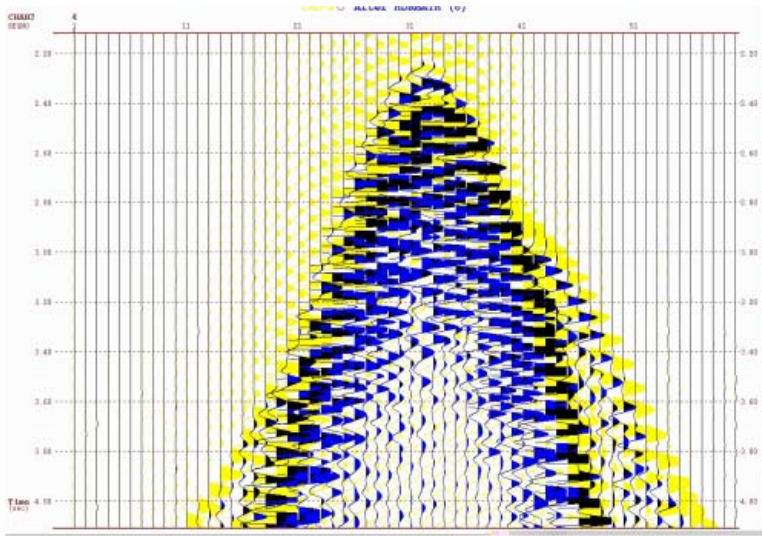
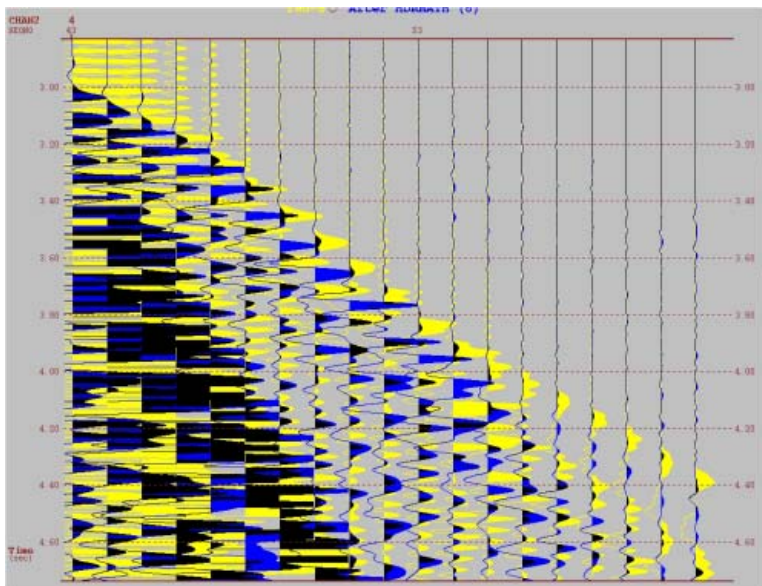


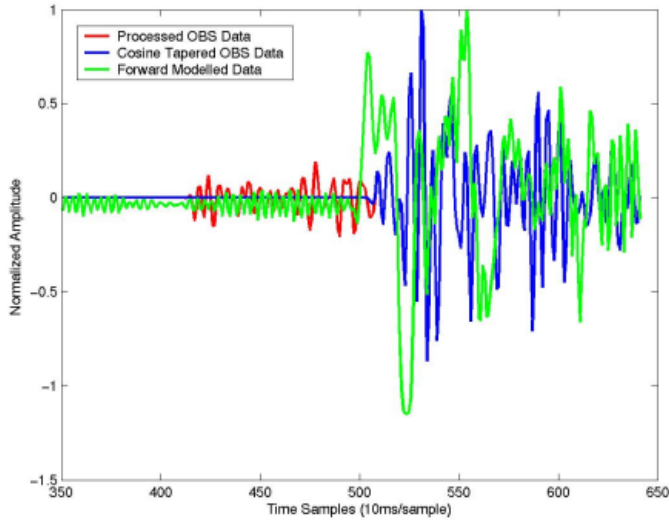
Figure 15(a) : Inverted velocity model after one iteration at the lowest frequency (2Hz), when no filtering parameters are used. All colors indicate velocity marked in m/s and x-z axis indicates distance in km. This figure demonstrates the importance of the correct inversion parameters in keeping the inversion stable. The offset weighting is very important to force the inversion to use the larger offset, crustal refracted data rather than the near-offset water wave data. Wavenumber filtering maintains the linearity of the problem. (b) : Inverted velocity model after one iteration at the lowest frequency when the SI units are used in the model. If at all iterations run, they give unrealistic updates like these (Refer text).



16(a)



16(b)



16(c)

Figure 16(a) : Overlay of the forward modeled synthetic seismogram (yellow) and the observed OBS seismogram from OBS 17(blue), the overlap is indicated by the black color. Visibly, the first arrival of the direct wave (near offsets) for both seismograms matches better than the seismic refracted arrivals (large offsets). The x axis features the shot numbers (1 through 61) for the receiver gather. A close up of the same is shown in Fig (b) that indicates the presence of energy, coherent through all the shots, that arrives before the large amplitude arrivals for the observed data (and it overlaps somewhat with the forward modeled data). This energy is the first arrival energy but its amplitude is almost the same as the experimental noise, it is only the coherence that identifies it to be a seismic first arrival and not just random noise. (c) Individual trace of OBS 55, Shot 60 to show the effect of the Cosine Taper in reducing the pre-first-pick noise in the observed dataset, in order to make the coherent first arrivals appear more distinct over the random noise. The first arrivals of observed and modeled data seem to be a better match now.

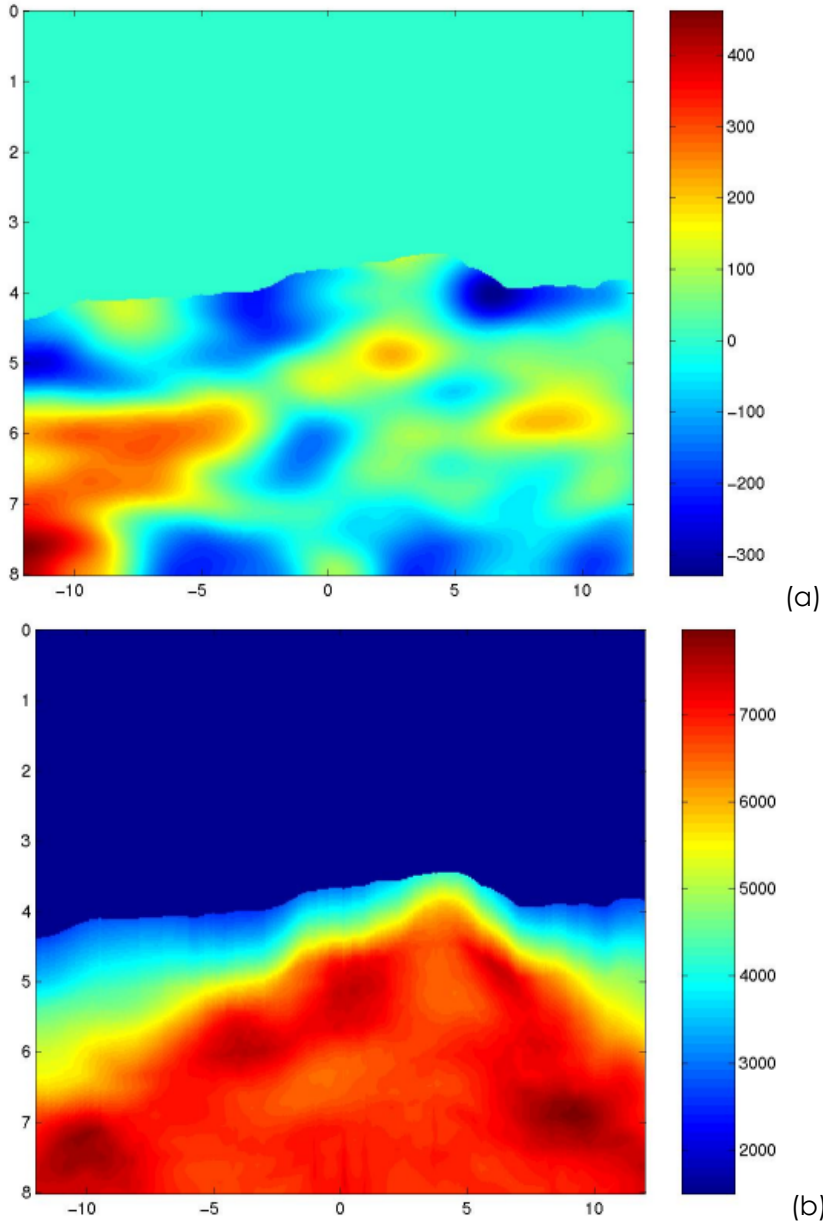
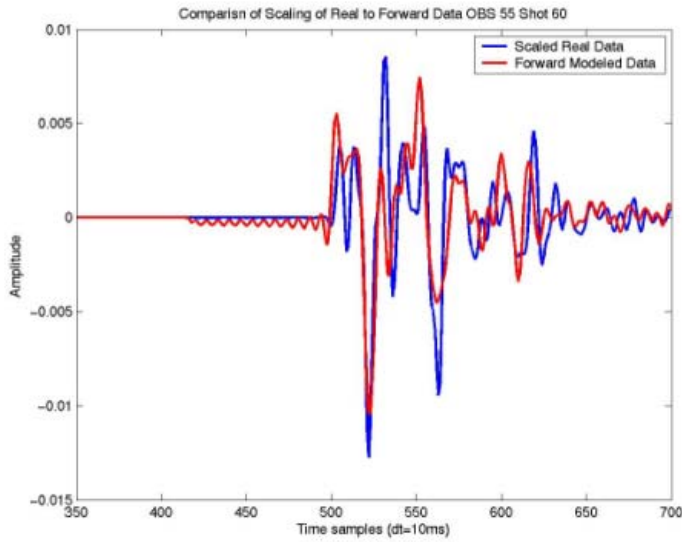
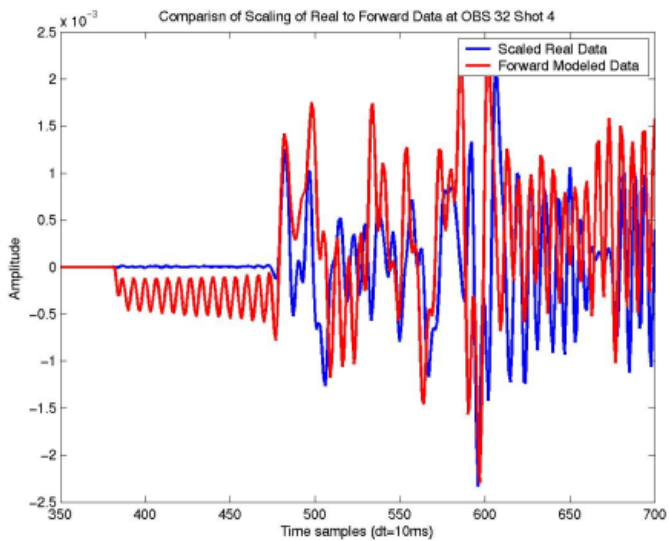


Figure 17(a) : Stochastic Velocity perturbation on the travelttime tomography model using Equation 11. All perturbations above the sea-floor topography are masked. All colors indicate velocity marked in m/s and x-z axis indicate distance in km. (b) Final velocity model after adding the perturbations to the TT model to get the synthetic model.



(a)



(b)

Figure 18(a) : The blue curve shows the forward modeled seismogram recorded on OBS 55 from Shot 60 using the stochastically computed velocity model (observed synthetic seismogram) and the red curve shows the same trace (OBS 55, Shot 60 : Far offsets) using the traveltimes tomography velocity model. Since the first arrival travel-time pick matches within a period, the latter velocity model is accurate as a starting model for Waveform Tomography using synthetically generated observed data and should give accurate results provided the acquisition sampling and associated parameters are correct. (b) Comparison of the first arrival picks for OBS 32, Shot 4 which resulted in the same interpretation as (a).

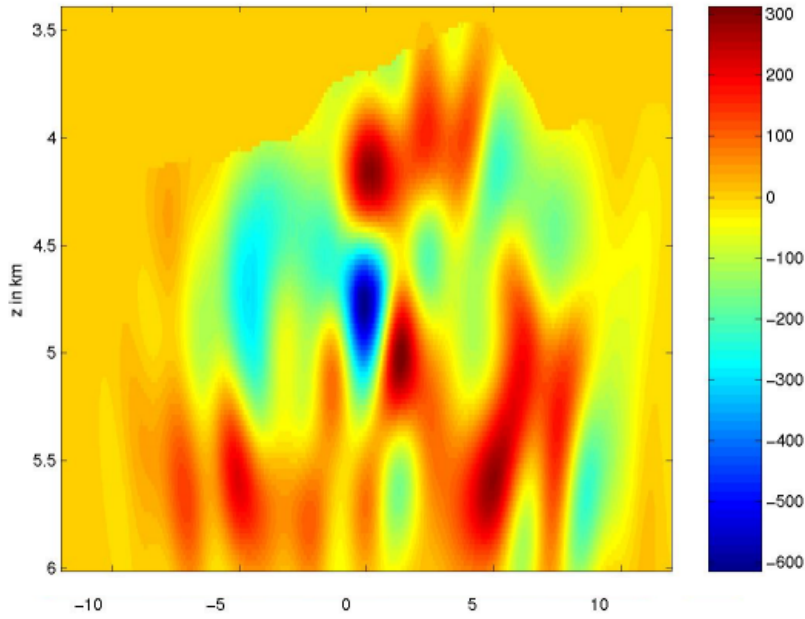


Figure 19 : Final velocity model (after inversion of 7 sequential frequencies using the traveltimes tomography model as the starting model and a synthetic seismograms computed on the stochastic model as the observed data) minus the starting model. All wavelengths above 2Km in depth and 5km laterally were inverted for, other inversion parameters remaining the same as before. This figure should ideally match Figure 17 (a) if the inversion process is accurate.